



**HAL**  
open science

## **NH<sub>3</sub> spatio-temporal variability over Paris, Mexico and Toronto and its link to PM<sub>2.5</sub> during pollution events**

Camille Viatte, Rimal Abeed, Shoma Yamanouchi, William Porter, Sarah Safieddine, Martin van Damme, Lieven Clarisse, Beatriz Herrera, Michel Grutter, Pierre-Francois Coheur, et al.

### ► To cite this version:

Camille Viatte, Rimal Abeed, Shoma Yamanouchi, William Porter, Sarah Safieddine, et al.. NH<sub>3</sub> spatio-temporal variability over Paris, Mexico and Toronto and its link to PM<sub>2.5</sub> during pollution events. Atmospheric Chemistry and Physics Discussions, 2022, pp.(Under Review). 10.5194/egusphere-2022-413 . insu-03695678v1

**HAL Id: insu-03695678**

**<https://insu.hal.science/insu-03695678v1>**

Submitted on 15 Jun 2022 (v1), last revised 26 Oct 2022 (v2)

**HAL** is a multi-disciplinary open access archive for the deposit and dissemination of scientific research documents, whether they are published or not. The documents may come from teaching and research institutions in France or abroad, or from public or private research centers.

L'archive ouverte pluridisciplinaire **HAL**, est destinée au dépôt et à la diffusion de documents scientifiques de niveau recherche, publiés ou non, émanant des établissements d'enseignement et de recherche français ou étrangers, des laboratoires publics ou privés.



Distributed under a Creative Commons Attribution - NonCommercial 4.0 International License



1 **NH<sub>3</sub> spatio-temporal variability over Paris, Mexico and Toronto and its link to**  
2 **PM<sub>2.5</sub> during pollution events**

3

4 Camille Viatte<sup>1</sup>, Rimal Abeed<sup>1</sup>, Shoma Yamanouchi<sup>2,3</sup>, William Porter<sup>4</sup>, Sarah Safieddine<sup>1</sup>, Martin Van  
5 Damme<sup>5,6</sup>, Lieven Clarisse<sup>4</sup>, Beatriz Herrera<sup>2,7</sup>, Michel Grutter<sup>7</sup>, Pierre-Francois Coheur<sup>4</sup>, Kimberly  
6 Strong<sup>2</sup>, and Cathy Clerbaux<sup>1,5</sup>.

7 <sup>1</sup>LATMOS/IPSL, Sorbonne Université, UVSQ, CNRS, 75252 Paris Cedex 05, France;

8 <sup>2</sup>Department of Physics, University of Toronto, Toronto, ON M5S 1A7, Canada;

9 <sup>3</sup>Department of Civil and Mineral Engineering, University of Toronto, Toronto ON M5S 1A4, Canada;

10 <sup>4</sup>Department of Environmental Sciences, University of California, Riverside, CA 92521, USA;

11 <sup>5</sup>Université libre de Bruxelles (ULB), Spectroscopy, Quantum Chemistry and Atmospheric Remote Sensing (SQUARES), Brussels 1050,  
12 Belgium;

13 <sup>6</sup>BIRA-IASB - Belgian Institute for Space Aeronomy, Brussels 1180, Belgium;

14 <sup>7</sup>Instituto de Ciencias de la Atmósfera y Cambio Climático, Universidad Nacional Autónoma de México, Mexico City, 04510, Mexico;

15 *Correspondence:* Camille Viatte ([camille.viatte@latmos.ipsl.fr](mailto:camille.viatte@latmos.ipsl.fr))



16 **Abstract**

17 Megacities can experience high levels of fine particulate matter (PM<sub>2.5</sub>) pollution linked to ammonia  
18 (NH<sub>3</sub>) mainly emitted from agricultural activities. Here, we investigate such pollution in the cities of  
19 Paris, Mexico and Toronto, each of which have distinct emission sources, agricultural regulations, and  
20 topography. Ten years of measurements from the Infrared Atmospheric Sounding Interferometer  
21 (IASI) are used to assess the spatio-temporal NH<sub>3</sub> variability over and around the three cities.

22 In Europe and North America, we determine that temperature is associated with the increase in NH<sub>3</sub>  
23 atmospheric concentrations with coefficient of determination ( $r^2$ ) of 0.8 over agricultural areas. The  
24 variety of the NH<sub>3</sub> sources (industry and agricultural) and the weaker temperature seasonal cycle in  
25 southern North America induce a lower correlation factor ( $r^2 = 0.5$ ). The three regions are subject to  
26 long range transport of NH<sub>3</sub>, as shown using HYSPLIT cluster back-trajectories. The highest NH<sub>3</sub>  
27 concentrations measured at the city scales are associated with air masses coming from the  
28 surrounding and north-northeast regions of Paris, the south-southwest areas of Toronto, and the  
29 southeast/southwest zones of Mexico City.

30 Using NH<sub>3</sub> and PM<sub>2.5</sub> measurements derived from IASI and surface observations from 2008 to 2017,  
31 annually frequent pollution events are identified in the 3 cities. Wind roses reveal statistical patterns  
32 during these pollution events with dominant northeast-southwest directions in Paris and Mexico  
33 cities, and the transboundary transport of pollutants from the United-States in Toronto. To check  
34 how well chemistry transport models perform during pollution events, we evaluate simulations made  
35 using the GEOS-Chem model for March 2011. In these simulations we find that NH<sub>3</sub> concentrations  
36 are overall underestimated, though day-to-day variability is well represented. PM<sub>2.5</sub> is generally  
37 underestimated over Paris and Mexico, but overestimated over Toronto.



## 38 1. Introduction

39 Paris, Toronto, and Mexico City are cities with over 2 million inhabitants. When their larger  
40 metropolitan regions are included, their populations are 10.5 million for Paris (the most populous  
41 area in the European Union), 6.5 million for Toronto (the fourth most populous city in North  
42 America) and 9.2 million for Mexico City (most populous city in North America). These cities typically  
43 experience strong particulate matter (PM) pollution episodes. Exposure to such particles is harmful  
44 to humans and can lead to cardiovascular and respiratory diseases [Murray et al., 2020].

45 A large proportion of the particles' composition is ammonium sulfate and nitrate, which are formed  
46 from ammonia (NH<sub>3</sub>) [Behera et al., 2013] released in the atmosphere from e.g., fertilizer spreading  
47 practices and both transported to cities, reducing the quality of urban air [Pope et al., 2009]. The  
48 agricultural sector represents 94%, 90%, and 94% of total NH<sub>3</sub> emissions in France [CITEPA, 2018],  
49 Canada [ECCC, 2017] and Mexico [INECC and SEMARNAT, 2018], respectively. NH<sub>3</sub> is the most poorly  
50 understood precursor of PM<sub>2.5</sub> (PM with a diameter less than 2.5 μm), primarily because  
51 measurements are difficult [von Bobruzki et al., 2010], sparse, and due to low ambient NH<sub>3</sub>  
52 concentrations and episodic emissions. Worldwide, only five countries have included NH<sub>3</sub>  
53 concentrations routine measurements in their air quality monitoring networks [Nair and Yu, 2020].

54 NH<sub>3</sub> emissions are associated with very high uncertainties in all inventories (186% to 294%  
55 uncertainties in EDGAR [McDuffie et al., 2020; Van Damme et al., 2018]) due to uncertainties in the  
56 reporting of agricultural statistics and emission factors that depend on individual agricultural  
57 practices, biological processes, and environmental conditions [Paulot et al., 2014], as well as political  
58 disturbances and land-use change [Abeed et al., 2021]. The evaporation of NH<sub>3</sub> in the atmosphere, as  
59 well as its transformation into particulate matter, is highly dependent on the thermodynamic  
60 conditions of the atmosphere [Sutton et al., 2013]. All these parameters account for the complexity  
61 of reproducing NH<sub>3</sub> concentrations in atmospheric models, predicting the associated PM<sub>2.5</sub> pollution,  
62 and, ultimately, implementing relevant regulations to reduce its emissions.

63 Given the crucial role that NH<sub>3</sub> plays in environmental and public health problems, reducing its  
64 emissions will therefore be a major challenge. However, NH<sub>3</sub> concentrations are increasing in all of  
65 three regions, with a country wide increase of 24 ± 11%, 16.4 ± 8.6%, and 8.4 ± 5.2 % between 2008  
66 and 2018 in France, Canada, and Mexico, respectively [Van Damme et al., 2021].

67 In Paris, PM<sub>2.5</sub> are composed with organic matter (38–47 %), nitrate (17–22 %), non-sea-salt sulfate  
68 (13–16 %), ammonium (10–12 %), and to a minor extend with elemental carbon, mineral dust (2–5  
69 %) and sea salt [Bressi et al., 2013]. In springtime, it has been shown that NH<sub>3</sub> plays a significant role  
70 in PM<sub>2.5</sub> pollution episodes [Viatte et al., 2021] but long-term observations are needed to properly  
71 evaluate the impact of NH<sub>3</sub> to PM<sub>2.5</sub> formation.

72 In Toronto, secondary nitrate formed with nitric acids (NO<sub>x</sub>) and NH<sub>3</sub> account for 36% of the PM<sub>2.5</sub>  
73 sources [Lee et al., 2003] and ammonium nitrate and sulfate accounted for 20-30% of annual PM<sub>2.5</sub>  
74 mass over the 14-year period between 2006 and 2014 [Jeong et al., 2020]. There is a need for a  
75 higher number of surface observations to evaluate the NH<sub>3</sub>-PM<sub>2.5</sub> relationship and its evolution over  
76 time [Larios et al., 2018].

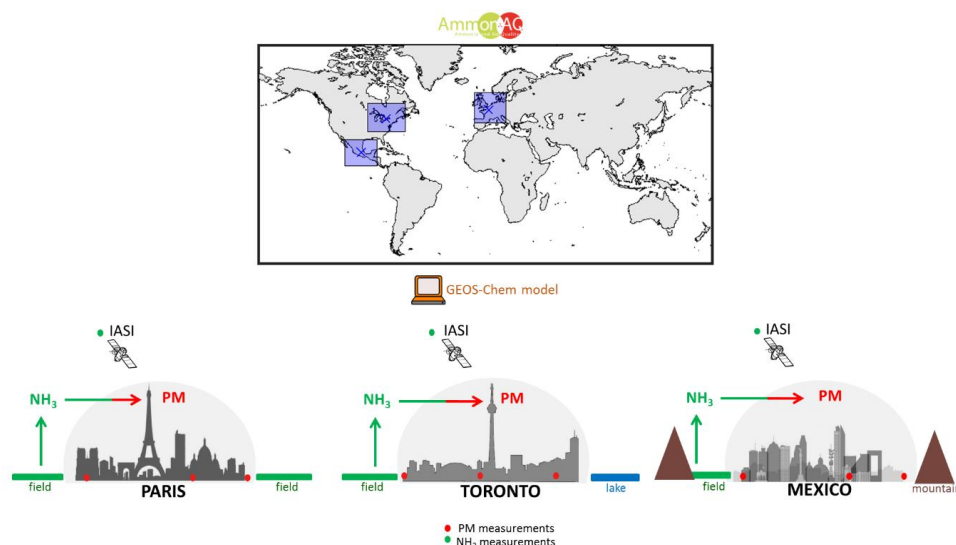
77 In Mexico, PM<sub>2.5</sub> concentrations often exceed the standard of 65 μg/m<sup>3</sup> [Moya and Huey, 2007;  
78 INECC and SEMARNAT, 2018]. Secondary inorganic aerosols account for 30% of the chemical  
79 composition of PM<sub>2.5</sub>, which are dominated by ammonium sulfate with an average of 14% [Vega et  
80 al., 2010]. A better understanding of the particulate pollutants processes in Mexico is still needed  
81 [Ojeda-Castillo et al., 2019].



82 To assess the role of  $\text{NH}_3$  in the formation of particulate matter, the AmmonAQ (Ammonia air  
83 quality) project was designed to quantify  $\text{NH}_3$  spatio-temporal variabilities in regional domains  
84 around these three cities. The main objective of this project is to determine the impact of intensive  
85 agricultural practices on  $\text{NH}_3$  and urban air quality, with a focus on Paris, Toronto and Mexico as  
86 benchmark case studies. A schematic representation of the AmmonAQ project and the domains of  
87 study are shown in Figure 1. The so-called “Europe”, “North America”, and “southern North America”  
88 domains represent the extended area with  $\text{NH}_3$  sources that can impact on the Paris, Toronto, and  
89 Mexico cities air composition. The three cities are investigated with the use of different datasets:  
90 satellite measurements and model simulation data, and surface measurements when available (see  
91 section 2).

92 These cities have been chosen as the focus of this study because of the availability of  $\text{NH}_3$  and  $\text{PM}_{2.5}$   
93 measurements. These three cities differ in terms of:

- 94 1. The regulation of  $\text{NH}_3$  emissions: French policies aim to reduce  $\text{NH}_3$  emissions by 13% in 2030  
95 relative to 2005 [CEIP, 2016] following EU ratification of the Gothenburg Protocol in 2017,  
96 whereas in Canada and Mexico there are no federal regulations for  $\text{NH}_3$  emissions yet  
97 [Bittman et al., 2017];
- 98 2. Agricultural practices affecting  $\text{NH}_3$  emissions differ in each region as farmers depend on  
99 meteorological conditions for fertilizer use;
- 100 3. Meteorological/climate conditions are very different in each of the regions: drier winter and  
101 wetter summer in Toronto compared to Paris, and weak winds and strong temperature  
102 inversions in Mexico-city. This influences the  $\text{NH}_3$  lifetime and chemistry leading to the  
103 formation of  $\text{PM}_{2.5}$ ;
- 104 4. Topography: Toronto is adjacent to Lake Ontario, Paris is inland, and Mexico-city is a basin  
105 surrounded by mountains. This will impact the trajectories of air masses.



106

107 Figure 1: schematic representation of the AmmonAQ project. Upper panel: the three study regions investigated  
108 (in blue rectangles). Lower panel: presentation of each city and regional domain and different datasets used.

109



## 110 2. Methodology

### 111 2.1. NH<sub>3</sub> observations derived from IASI

112 The Infrared Atmospheric Sounding Interferometer (IASI) was launched onboard the Metop-A/B/C  
113 satellites in 2006, 2012, and 2018, respectively [Clerbaux et al., 2009]. IASI provides twice daily total  
114 column measurements of NH<sub>3</sub> globally at 9:30 and 21:30 local solar time. With its polar orbit and a  
115 swath of 2400 km, IASI pixel size is 12 km in diameter at nadir. In this work, we use version 3 of the  
116 ANNI-NH<sub>3</sub> product [Van Damme et al., 2021; Guo et al., 2021] from IASI Metop-A/B morning  
117 overpasses over the period 2008 to 2017.

### 118 2.2. PM<sub>2.5</sub> dataset derived from surface network measurements

119 To study local scale PM<sub>2.5</sub> pollution events in the Paris, Toronto, and Mexico cities, PM<sub>2.5</sub> observations  
120 of surface concentrations from 2008 to 2017 are used.

121 For Paris, we use hourly observations of PM<sub>2.5</sub> concentrations derived from fourteen stations of the  
122 Airparif network (<https://data-airparif-asso.opendata.arcgis.com/>). For Toronto, we analyze hourly  
123 PM<sub>2.5</sub> observations derived from eleven stations supported by the Ministry of the Environment,  
124 Conservation and Parks of Ontario (<http://www.airqualityontario.com/>). For Mexico, PM<sub>2.5</sub>  
125 concentrations are derived from 27 stations of the Red Automática de Monitoreo Atmosférico  
126 (RAMA, <http://www.aire.cdmx.gob.mx/default.php?opc=%27aKBh%27>) network.

127 All these stations are located in a 50-km radius-circle around the city centers of Paris, Toronto, and  
128 Mexico City.

### 129 2.3. NH<sub>3</sub> and PM<sub>2.5</sub> from the GEOS-Chem model

130 We generate model outputs for March of 2011 using version 12.7.2 of the GEOS-Chem chemical  
131 transport model [Bey et al., 2001] driven by the MERRA-2 reanalysis product, including nested  
132 domains over Europe and North America at a 0.5° × 0.625° horizontal resolution from which we  
133 extract modeled surface values for each city. Boundary conditions for these two nested domains are  
134 created using a global simulation for the same months at 2° × 2.5° resolution. Output for the  
135 analyzed month of March includes monthly means, as well as hourly means for selected diagnostics,  
136 and is preceded by two months of discarded model spinup time for the global simulation, and one  
137 month for each nested run. Anthropogenic emissions are taken primarily from the global Community  
138 Emissions Data System (CEDS) inventory [Hoesly et al., 2018], with regional emissions from the 2011  
139 National Emissions Inventory produced by the US EPA (NEI2011) used to override global values over  
140 the United States. Biogenic non-agricultural ammonia, as well as ocean ammonia sources, are taken  
141 from the Global Emission Inventories Activities database (GEIA, [Bouwman et al., 1997]). Open fire  
142 emissions are generated using the GFED 4.1s inventory [Randerson et al., 2017]. Sulfate-nitrate-  
143 ammonium aerosol processes are calculated using version 2.2 of the ISORROPIA thermodynamic  
144 module [Fountoukis and Nenes, 2007]. Black carbon is handled as described in Wang et al. (2014),  
145 while secondary organic aerosol is produced using the simplified irreversible scheme described in Pai  
146 et al., (2020).

### 147 2.4. Back-trajectories analysis from the HYSPLIT model

148 To determine the effect of long-range transport affecting the local air quality of the three cities, we  
149 use the Hybrid Single-Particle Lagrangian Integrated Trajectory model (HYSPLIT, [Stein et al., 2015]).  
150 One note that unlike the GEOS-Chem model, HYSPLIT does not include atmospheric chemistry. For  
151 the runs, meteorological data are from the National Centers for Environmental Prediction (NCEP) /



152 National Center for Atmospheric Research (NCAR) reanalysis at 2.5-degree global latitude-longitude  
 153 projection. First, we run daily 24-hours back-trajectories ending in the city-centers at the overpass  
 154 time of the IASI instrument covering the period 2008 to 2017. Then, for each day we calculate the  
 155 mean of  $\text{NH}_3$  total columns derived from IASI observations in a 50-km radius circle around the cities  
 156 associated with each back-trajectory. Finally, every back-trajectory are combined in clusters and  
 157 associated with the corresponding local-scale IASI  $\text{NH}_3$  concentrations.

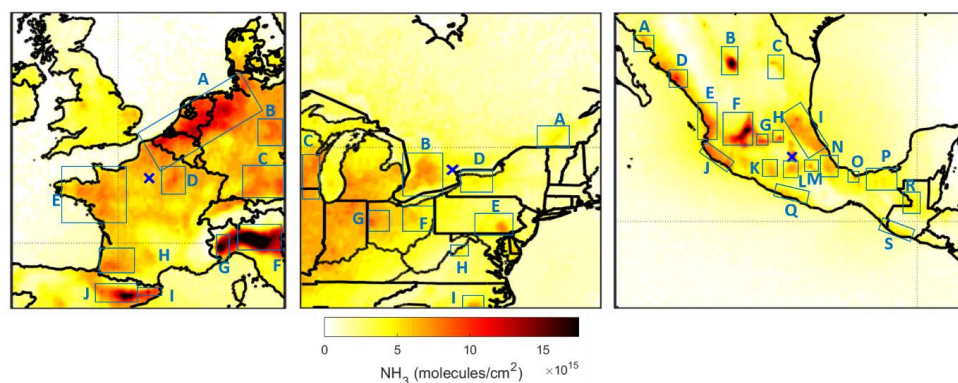
## 158 2.5. ERA-5 meteorological data

159 The meteorological variables used in this study are extracted from the hourly ECMWF's reanalysis  
 160 (ERA5, [Hersbach et al., 2020]). ERA5 data are at  $0.25^\circ \times 0.25^\circ$  resolution (native horizontal resolution  
 161 of ERA5 is  $\sim 31\text{km}$ ) and are interpolated in time and space to the IASI observation. The meteorological  
 162 parameters considered here are the skin temperature ( $T_{\text{skin}}$ , which is the physical temperature of  
 163 the Earth's surface), total precipitation (in meter of water equivalent - accumulated liquid and frozen  
 164 water, comprising rain and snow -) and relative humidity up to 2 meters above the surface calculated  
 165 from dew and air temperature at 2m from ERA5.

## 166 3. Results

### 167 3.1. $\text{NH}_3$ source regions identification and spatio-temporal variability over the Europe, 168 North America, and southern North America domains

169 Using 10-years of IASI observations, the main source regions of  $\text{NH}_3$  in the 3 domains of study are  
 170 identified (Figure 2) and listed in Table 1. We identify 10, 9, and 19  $\text{NH}_3$  source regions over the  
 171 Europe, North America, and southern North America regions, respectively. All of the sources over the  
 172 Europe, North America domains are mostly related to agricultural practices (farming and spreading  
 173 practices). This is in agreement with previous calculation of worldwide nitrogen inputs from fertilizer  
 174 and manure [Potter et al., 2010]. Around southern North America, three sources are related to  
 175 fertilizer or soda ash industries (listed with C, G, O in Figure 2 and Table 1, [Van Damme et al., 2018]),  
 176 the rest is agricultural.



177  
 178 Figure 2: Source region identification of  $\text{NH}_3$  derived from 10 years average of IASI total columns  
 179 ( $\text{molecules/cm}^2$ ) from 2008 to 2017. The blue crosses indicate Paris, Toronto, and Mexico cities locations.

180 Spatio-temporal variabilities of  $\text{NH}_3$  in the atmosphere in the three regions (Figure 2) are not  
 181 expected to be similar:  $\text{NH}_3$  emissions from industries in the region of southern North America are  
 182 released all year long, whereas  $\text{NH}_3$  emissions from agricultural practices (i.e. major over Europe and  
 183 North America), depend on various surface and meteorological conditions. In order to investigate



184 this, NH<sub>3</sub> concentrations using 10-years of IASI observations are assessed against atmospheric  
 185 temperature and precipitation derived from the ERA5 reanalysis over the three domains in Figure 3.  
 186 It shows the seasonal evolution of NH<sub>3</sub> from IASI over the three regions (left panel), along with the  
 187 seasonal evolution of temperature and precipitation (right panel).

188 Table 1: List of NH<sub>3</sub> source regions identified using 10-years average of IASI total columns (molecules/cm<sup>2</sup>) over  
 189 the Europe, North America, and southern North America regions.

Europe [41°-59°N ; -11.25°- 16.25°E]		North America [35°-53°N ; 93.75°-63.75°W]		Southern North America [9°-29°N ; 113.75°-86.25°W]	
A	The North-European plain <sup>1,2</sup>	A	Granby	A	Obregon (Mexico) <sup>1</sup>
B	Saxe Anhalt plain (Germany)	B	Elmira-Kitchener-Guelph	B	Torreón (Mexico) <sup>1,2</sup>
C	Munich - Mangfall (Germany)	C	Brillion area	C	García (Mexico)** <sup>1</sup>
D	Champagne-Ardennes (France)	D	New-York state	D	Culiacancito (Mexico) <sup>1,2</sup>
E	Bretany-Pays de la Loire (France) <sup>2</sup>	E	Lancaster county	E	Nayarit (Mexico)
F	Pô Valley (Italy) <sup>1,2</sup>	F	Wayne county	F	Jalostotitlan-San Juan de Los Lagos (Mexico) <sup>1,2</sup>
G	Valley of piedmont (Italy) <sup>1,2</sup>	G	Celina-Coldwater <sup>1</sup>	G	Salamanca – Villagran (Mexico)* <sup>1</sup>
H	Landes area (France)	H	Shenandoah Valley- Bridgewater <sup>1</sup>	H	Ezequiel Montes (Mexico) <sup>1,2</sup>
I	Vic - Manlleu (Spain) <sup>1,2</sup>	I	Lenoir County	I	Tampaon, Loma Alta (Mexico) <sup>1</sup>
J	Ebro river basin (Spain) <sup>1,2</sup>			J	Tecoman (Mexico)
				K	Coyuca de Catalan (Mexico)
				L	Morelos (Mexico)
				M	Tochtepec-Tehuacan (Mexico) <sup>1</sup>
				N	South of Veracruz (Mexico)
				O	Cosolaecaque (Mexico)* <sup>1</sup>
				P	Tabasco (Mexico)
				Q	Guerrero (Mexico)
				R	Chisec (Guatemala)
				S	Texcuaco (Guatemala)

\*Fertilizer industry \*\* Soda ash industry

<sup>1</sup> Van Damme et al., 2018; Clarisse et al., 2019

<sup>2</sup> Dammers et al., 2019

190

191 For Europe and North America, NH<sub>3</sub> total columns are the highest in spring and summer. In fact, NH<sub>3</sub>  
 192 concentrations over Europe exhibit two seasonal maxima in March/April and July/August  
 193 (supplementary material, Figure S1) and in North America the maxima are in May and September  
 194 (Figure S2). This is consistent with agricultural practices (i.e. fertilizer application) and higher air  
 195 temperature favoring NH<sub>3</sub> volatilization in the atmosphere.

196 The right panel of Figure 3 shows how temperature (red lines) and precipitation (blue bars)  
 197 seasonally evolve over the three regions. In winter, atmospheric temperatures are below 5 °C in  
 198 Europe and North America, and IASI observations reveal almost no NH<sub>3</sub> hot spots (left panel, Figure  
 199 3). This can be due to the lack of NH<sub>3</sub> abundance, lower volatilization in this temperature range, no  
 200 agricultural emissions in winter and/or the reduced sensitivity of the IASI NH<sub>3</sub> retrievals in winter  
 201 [Van Damme et al., 2017].

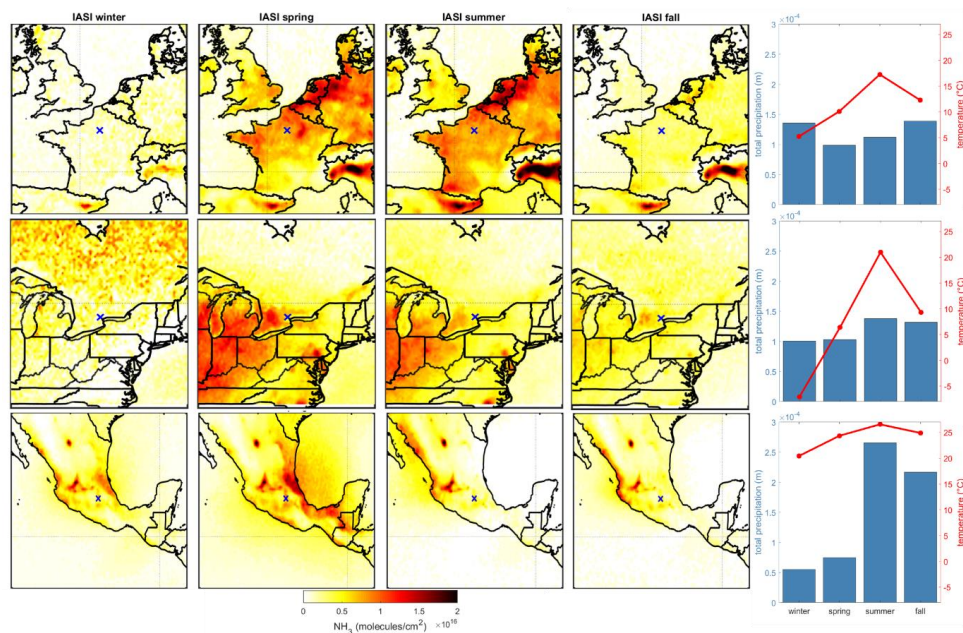
202 In southern North America, NH<sub>3</sub> seasonal variations are less pronounced than in the other two  
 203 regions. Figure 3 shows that the NH<sub>3</sub> concentrations over several sources, such as Torreón and San  
 204 Juan de Los Lagos (boxes B and F in Figure 2 right panel) are high during all seasons, which could be  
 205 associated with the weak seasonal cycle of temperature in this region close to the equator.

206 In spring, seasonal precipitations are the lowest for the three regions. This is reflected in high NH<sub>3</sub>  
 207 concentrations on the left panel. Over Europe and North America, this can be related to agricultural  
 208 spreading practices period and higher atmospheric temperature favoring NH<sub>3</sub> volatilization. In  
 209 southern North America, NH<sub>3</sub> concentrations observed by IASI are the highest in spring when  
 210 atmospheric temperatures are high and precipitations rates are low. In addition, biomass burning,





211 that are often encountered during this period could explain higher atmospheric NH<sub>3</sub> concentrations  
 212 in spring. NH<sub>3</sub> reach maximum values in April/May (Figure S3) just before the start of the rain season,  
 213 potentially reducing observed NH<sub>3</sub> concentrations due to the wet deposition of atmospheric gaseous  
 214 ammonia [Asman et al., 1998].



215

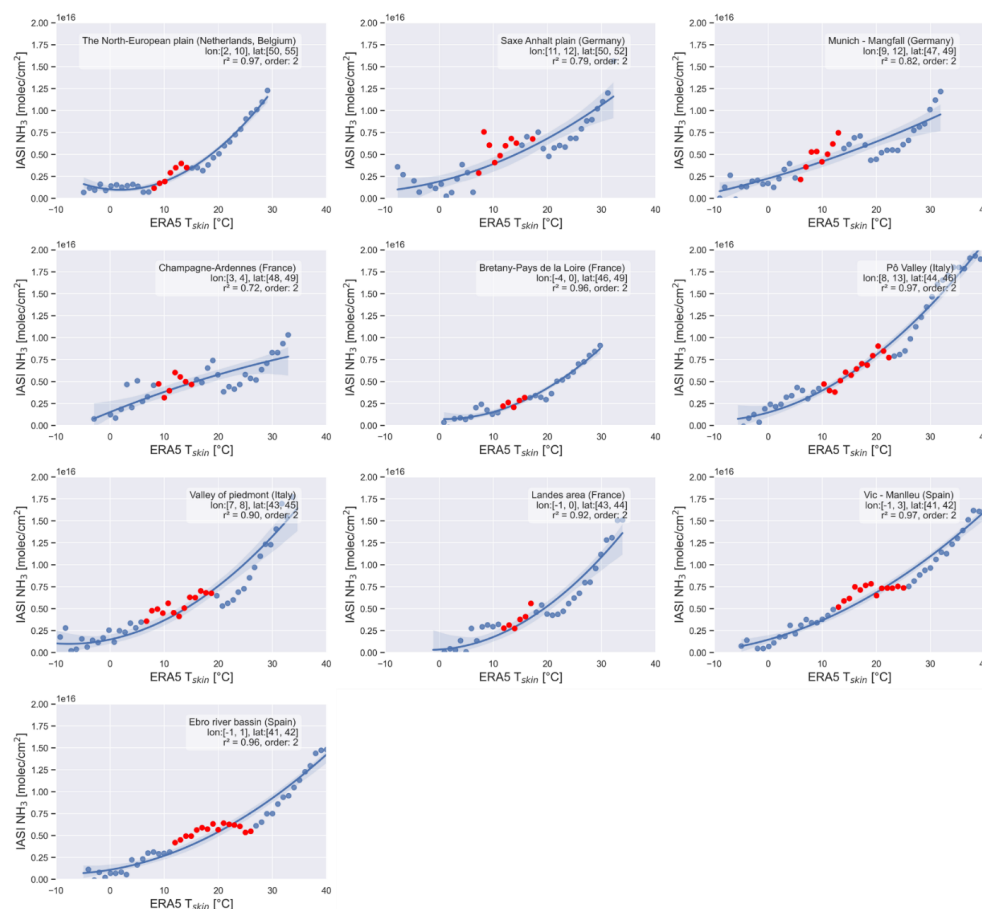
216 Figure 3: Seasonal maps of NH<sub>3</sub> total columns (molecules/cm<sup>2</sup>) derived from 10 years (2008-2017) of IASI  
 217 observations, along with seasonal means of atmospheric temperature (red line) and precipitation (blue bar  
 218 chart) over the Europe (upper panels), North America (middle panels), and southern North America (lower  
 219 panels) regions.

220 Since in Europe and North America NH<sub>3</sub> sources are mostly agriculture-related (with a mild  
 221 contribution from industries), the temperature/NH<sub>3</sub> relationship is expected to be relatively easy to  
 222 interpret: when the land surface temperature increases, volatilization of ammonia from the  
 223 fertilized/manured soil is favored, and atmospheric ammonia increases. The corresponding  
 224 determination factors  $r^2$  for this relationship in Europe and North America are 0.85 and 0.80  
 225 respectively (polynomial fit of second order). This is not the case in southern North America, in which  
 226 some of the ammonia sources are also industrial and they contribute greatly to the atmospheric NH<sub>3</sub>,  
 227 the concentrations of ammonia are therefore not directly temperature dependent, as we can see on  
 228 the right upper panel in Figure S4 ( $r^2 = 0.46$ ). There is nonetheless a relationship in southern North  
 229 America that is due to the fact that we have constant high ammonia sources and temperatures  
 230 (Figure 3). In fact, the relationships between NH<sub>3</sub> and temperature on one hand, and  
 231 precipitation/relative humidity on the other hand, are not linear; this has been equally shown in a  
 232 previous study [Sutton et al., 2013].

233 To further investigate the temperature/NH<sub>3</sub> relationship, we show in Figure 4 the evolution of NH<sub>3</sub>  
 234 with respect to land surface temperature over different sub-regions of the Europe domain (listed in  
 235 Table 1). Similar Figures for the North America and southern North America domains are shown in  
 236 the supplement information (Figure S5 and S6). We observe a peak of NH<sub>3</sub> followed by a local



237 maximum plateau between 10 and 25°C approximately in all of the regions of the Europe domain  
 238 (Figure 4). In fact, the NH<sub>3</sub> detected in this range of temperature can indicate the fertilizer application  
 239 period, since most of them (up to 80%) were detected during the spring and fall seasons. For  
 240 instance, over the Po valley (region F in Table 1, Figure 4), 36% of the NH<sub>3</sub> detected in the bins 10 –  
 241 25°C correspond to the spring season, whereas 35% correspond to the fall season (not shown here).  
 242 In Celina-Coldwater (region G in Table 1), 82% of the NH<sub>3</sub> detected between 10 and 25°C correspond  
 243 to the spring and the fall seasons, the percentage is split equally (Figure S5).



244 Figure 4: Yearly IASI NH<sub>3</sub> total columns (molecules/cm<sup>2</sup>) averaged per bins of ERA5 skin temperatures (°C), with  
 245 an interval of 1°C between each consecutive bin. The red circles denote the growing seasons, at least 60% of  
 246 the NH<sub>3</sub> is detected during March-May and Sept-Nov periods. See Figure 2 and Table 1 for the localization of  
 247 the sub-regions around Europe.  
 248

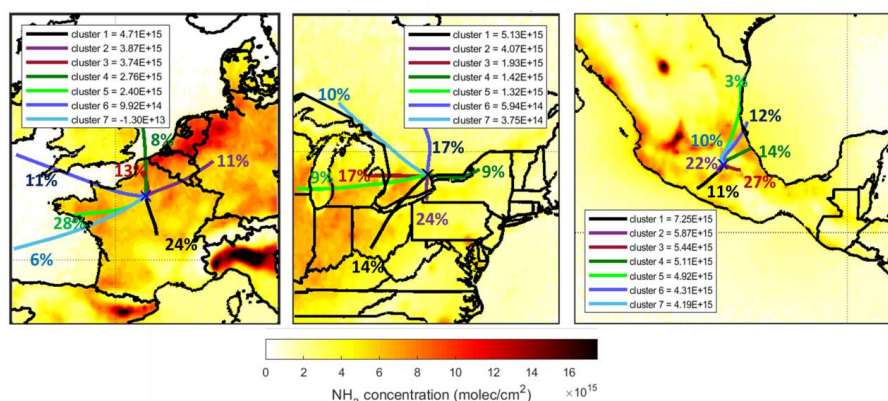
249 We choose to show the sub regions in the vicinity of the Europe domain, since they are mostly  
 250 agricultural sources. The “bumps” corresponding to the fertilizer application are very clear in all of  
 251 the sub-regions. This bump was detected to a lower extent for agricultural regions affecting North  
 252 America (supplementary material Figure S5). Over the agricultural regions in the southern North  
 253 America domain, the bumps are clear in the regions A to D (Figure S6, a). When the seasonal  
 254 temperatures do not fluctuate during the fertilizer application, any increase in atmospheric NH<sub>3</sub> is



255 due to the sudden addition of nitrogen fertilizers in the soil. In southern North America, the regions E  
 256 to M show that the highest  $\text{NH}_3$  concentrations were observed as the temperature increased during  
 257 the growing seasons (Figure S6). A possible explanation to the resemblance among the regions A to D  
 258 is that they share similar climate properties (Steppe and Desert) unlike the rest of the sub-regions in  
 259 the same domain (tropical/subtropical). Since the temperatures in the Europe and southern North  
 260 America domains are higher (Figure 3, right panels) in spring and fall seasons (fertilizer application  
 261 period) than those in North America, this bump is clearer in the latter. The bumps seen for the  
 262 Europe regional domain are clearer than those of southern North America, possibly related to the  
 263 fact that in autumn in Europe precipitation is lower than those in southern North America, leading to  
 264 lower  $\text{NH}_3$  loss through wet deposition.

### 265 3.2. $\text{NH}_3$ budget over the cities of Paris, Toronto, and Mexico

266 Temperature, relative humidity, and precipitation are not the only factors affecting the  $\text{NH}_3$   
 267 concentrations. More locally, and to analyze the impact of long-range transport on  $\text{NH}_3$   
 268 concentrations measured over the cities (and not domains) of Paris, Toronto, and Mexico, HYSPLIT  
 269 back-trajectories have been used. For each day of IASI  $\text{NH}_3$  observations made in a 50-km radius  
 270 circle from the city-center, a 24-hours back-trajectory has been performed from 2008 to 2017. There  
 271 are between 3643 and 4008 back-trajectories for Paris, Toronto, and Mexico cities. Then, a seven-  
 272 cluster analysis has been applied to these datasets and  $\text{NH}_3$  mean concentrations measured inside  
 273 the cities by IASI have been allocated to the different mean cluster trajectories. The result is shown in  
 274 Figure 5.



275

276 Figure 5: Seven cluster-mean backward trajectories over the Europe, North America, and southern North  
 277 America regions for the whole time period between 2008 and 2017. Back-trajectories are color-coded in  
 278 function of the corresponding  $\text{NH}_3$  concentrations measured inside the cities. The numbers indicate the  
 279 percentage of trajectories allocated to a cluster.

280 For Paris, 1/4 of all back-trajectories (875) that are associated with the most  $\text{NH}_3$  concentrations, i.e.  
 281  $4.71 \times 10^{15}$  molecules/cm<sup>2</sup> on average, are coming from the surrounding south regions (black line,  
 282 Figure 5). Clusters 2 and 3 are also associated with high  $\text{NH}_3$  concentrations and are coming from the  
 283 north-northeast. This is consistent with previous analyses using HYSPLIT [Viatte et al., 2020] and  
 284 FLEXPART models [Viatte et al., 2021]. As expected, the back-trajectories coming from the ocean are  
 285 related with almost no  $\text{NH}_3$  concentrations (light and dark blue lines, left panel).



286 Over Toronto, the highest  $\text{NH}_3$  concentrations (24% and 14%) measured in the city are allocated to  
 287 long-range transport located south-southwest (black and purple lines, middle panel) coming from the  
 288 United-States where most of the feedlots are. 9 to 17% of  $\text{NH}_3$  concentrations are coming from the  
 289 west and the east of Toronto (cluster 3, 4, and 5) where sources emissions have increased in the last  
 290 decade [Yao and Zhang, 2019]. The 2 back-trajectory clusters that are related to low  $\text{NH}_3$   
 291 concentrations are coming from the north (light and dark blue lines) where no  $\text{NH}_3$  sources have  
 292 been identified.

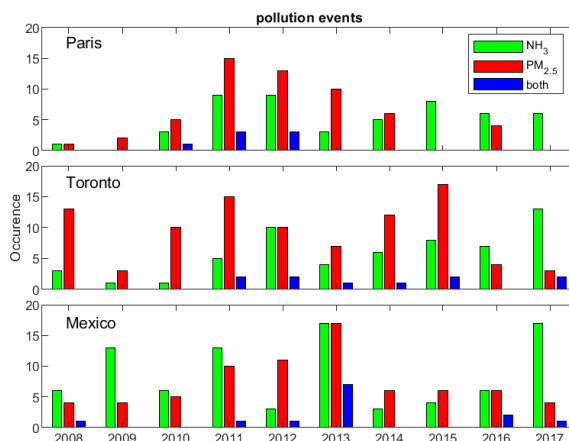
293 In the southern North America domain, back-trajectories are coming from relatively close regions  
 294 since orographic conditions around Mexico-city limit long-range transport. In this city, the highest  
 295  $\text{NH}_3$  concentrations are associated with air masses coming from the southwest (11%, black line, 22%,  
 296 purple line, right panel) and southeast (27%, red line). Air parcels coming from the north are  
 297 associated with relatively low  $\text{NH}_3$  concentrations measured in Mexico City.

### 298 3.3. Pollution events over Paris, Toronto, and Mexico cities from 2008 to 2017

299 After assessing the  $\text{NH}_3$  distribution under average climate conditions, we focus now on pollution  
 300 events occurring at the 3 cities. These are identified by applying the Fourier series of order 3  
 301 [Yamanouchi et al., 2021; Herrera et al., 2022] on the surface  $\text{PM}_{2.5}$  and satellite  $\text{NH}_3$  observations at  
 302 cities scale (i.e. 50-km radius circle from city-centers). The Fourier fit accounts for the “natural”  
 303 variability (seasonality) in the time-series, and helps identify pollution events that are above this  
 304 natural variability. It is a robust method commonly used to quantify trends and identify  
 305 enhancements in long-term timeseries [Zellweger et al., 2009]. Pollution events occurrence per year  
 306 and per city are shown in Figure 6.

307 The figure shows that  $\text{NH}_3$  pollution episodes are found to be annually frequent at the 3 cities. In  
 308 Toronto and Mexico cities,  $\text{PM}_{2.5}$  pollution events are encountered annually (with higher number in  
 309 Mexico) whereas no events are detected in 2009, 2015, and 2017 in Paris.

310 Numbers of identified days of  $\text{PM}_{2.5}$  pollution events are 88, 58, and 50 in Mexico City, Toronto, and  
 311 Paris, respectively. For  $\text{NH}_3$  pollution events, they occur more in Toronto than in Mexico City and  
 312 Paris, with number of days of 94, 73, and 56, respectively. Common days of high  $\text{NH}_3$  and  $\text{PM}_{2.5}$   
 313 concentrations are found in all 3 cities, especially in spring (not shown here), coinciding with the high  
 314 seasonal  $\text{NH}_3$  concentrations shown in Figure 3.





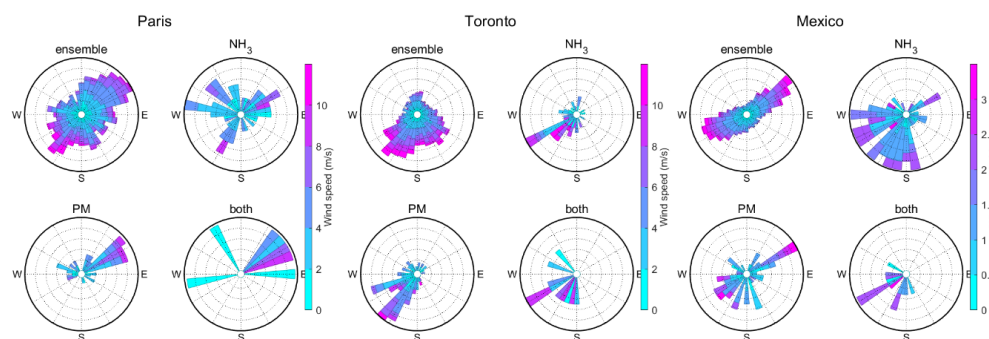
316 Figure 6: Annual occurrence of pollution events of NH<sub>3</sub> (green bars), PM<sub>2.5</sub> (red bars), and NH<sub>3</sub> and PM<sub>2.5</sub>  
 317 simultaneous (blue bars) detected from 2008 to 2017 in Paris (upper panel), Toronto (middle panel), and  
 318 Mexico (lower panel) cities.

319 To further investigate the impact of transport on pollution events occurring at the 3 cities, we have  
 320 analyzed the wind fields patterns for different cases: i) for the whole dataset (i.e. ensemble 2008-  
 321 2017), ii) for days of NH<sub>3</sub> and PM<sub>2.5</sub> pollution events occurred separately, and iii) for days when both  
 322 high concentrations are monitored. Figure 7 shows wind roses computed for the ensemble and these  
 323 different types of pollution events (i.e. PM<sub>2.5</sub>, NH<sub>3</sub> and both occurring during the same day). In  
 324 general, wind speed is lower at Mexico City (max 3 m.s<sup>-1</sup>) compared to Toronto and Paris (up to 10  
 325 m.s<sup>-1</sup>) because of the mountainous topography that blocks and slows air masses exchange in Mexico.

326 In Paris, the ensemble wind-roses show a dominant northeast-southwest pattern. NH<sub>3</sub> pollution  
 327 events are associated with wind coming from various directions at all wind speeds which was  
 328 suggested by the HYSPLIT cluster analysis (Figure 5), whereas PM<sub>2.5</sub> events are present mainly under  
 329 high northeast wind. When both NH<sub>3</sub> and PM<sub>2.5</sub> high concentrations are observed in Paris, the wind  
 330 field can have two patterns: low wind speed coming from all direction (except from the south) or  
 331 high wind speed coming from the northeast. This confirms the importance of transport of NH<sub>3</sub> and  
 332 PM<sub>2.5</sub> from the northeast and could suggest the inter-conversion of PM<sub>2.5</sub> to NH<sub>3</sub> at low wind speed.

333 In Toronto, the ensemble show that dominant wind pattern is coming from the south. For all the  
 334 pollution events (NH<sub>3</sub>, PM<sub>2.5</sub>, and both) the wind is coming from the southwest, confirming the long-  
 335 range transport of pollutants from the United-States.

336 In Mexico City, the dominant pattern (ensemble) is southwest-northeast wind fields. For days of NH<sub>3</sub>  
 337 pollution events, wind is mainly coming from the south-southwest, and for PM<sub>2.5</sub>, wind come from all  
 338 direction with an important northeast wind pattern. Days of both pollution events are associated  
 339 with wind coming from the west-southwest only.



340

341 Figure 7: Wind roses corresponding to the ensemble of all observations, the NH<sub>3</sub>, PM<sub>2.5</sub>, and both NH<sub>3</sub> and  
 342 PM<sub>2.5</sub> simultaneous pollution events derived from 2008 to 2017 over Paris (left panels), Toronto (middle  
 343 panels), and Mexico (right panels) cities.

### 344 3.4. Case study: NH<sub>3</sub> and PM<sub>2.5</sub> concentrations comparison with the GEOS-Chem model in 345 March 2011

346 The occurrence of pollution events varies from year to year (Figure 6). However, in 2011, all 3 cities  
 347 experienced PM<sub>2.5</sub> and NH<sub>3</sub> separate and combined pollution events. For this reason, GEOS-Chem



348 model simulations were performed in March 2011 to interpret the events and evaluate the model  
349 performance.

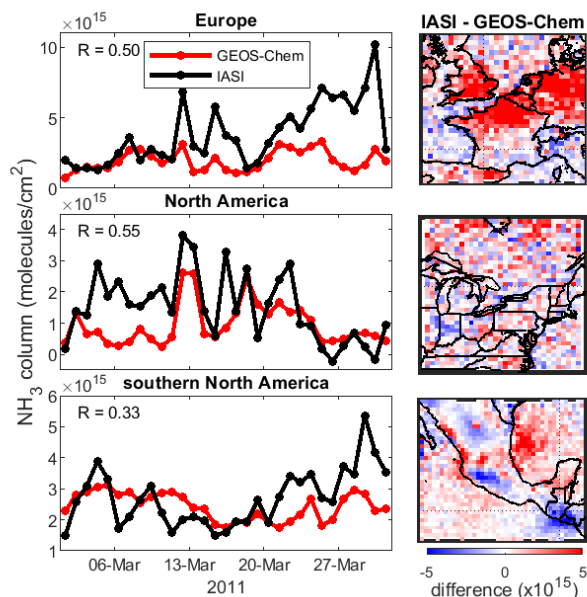
350 Spatial and temporal coincidence criteria have been applied to GEOS-Chem outputs to compare with  
351 IASI morning observations. We have selected collocated model outputs between 8.30 and 11.30 AM  
352 coincident with IASI overpasses. Averages of numbers of IASI observations are 1324, 1138, and 3000  
353 over the Europe, North America, and southern North America domains of study during March 2011.

354 Figure 8 shows the one-month comparison between the two datasets. Over the regional domains,  
355 the coefficient of correlation between daily model  $\text{NH}_3$  concentrations and IASI  $\text{NH}_3$  observations are  
356  $R = 0.50$ ,  $R = 0.55$ , and  $R = 0.33$ , over Europe, North America, and southern North America,  
357 respectively, with related  $p$ -values  $< 0.01$ .  $\text{NH}_3$  columns derived from the GEOS-Chem model are  
358 overall underestimated with Mean Relative Difference ( $\text{MRD} = (\text{observations} - \text{model}) / \text{model}$ ) of  
359 104%, 109%, and 12% over Europe, North America, and southern North America, respectively.

360 Over Europe and North America, day-to-day variabilities are in agreement since IASI and GEOS-Chem  
361 exhibit same enhancements (on March 12, 15, and 30 over Europe, and March 12, 13, and 18 over  
362 North America). In southern North America, the underestimation of the GEOS-Chem  $\text{NH}_3$  columns is  
363 less pronounced (MRD is 12%) than in the other regions but the day-to-day variability is not well  
364 represented in the model.

365 The GEOS-Chem model  $\text{NH}_3$  total columns are lower than those from IASI in March 2011 over specific  
366 locations in the southern North America and Europe domains (Figure 8, right panels). For the Europe  
367 region, GEOS-Chem  $\text{NH}_3$  columns are smaller than the IASI ones over the north of France, Belgium,  
368 the Netherlands, north of Spain (in particular sources A, B, C, D, E, I, and J of Figure 2) and the United  
369 Kingdom. For the southern North America domain, GEOS-Chem  $\text{NH}_3$  columns are smaller than the  
370 IASI ones over the west Mexican coast (sources A, D, E, J of Figure 2/Table 1), central (source F, G, H  
371 of Figure 2) and southeast (sources O and P of Figure 2) of Mexico City and over the Pacific Ocean,  
372 whereas they are higher in Guatemala (source S, R of Figure 2), and West of Mexico City.

373 Over the North America domain, spatial distribution of the differences between  $\text{NH}_3$  columns derived  
374 from GEOS-Chem and IASI are less pronounced than in the Europe and southern North America  
375 domains. IASI  $\text{NH}_3$  columns are smaller than GEOS-Chem outputs over the south of the United-States  
376 and over the Lancaster County (sources E and I of Figure 2) and higher over Indiana in the United  
377 States.

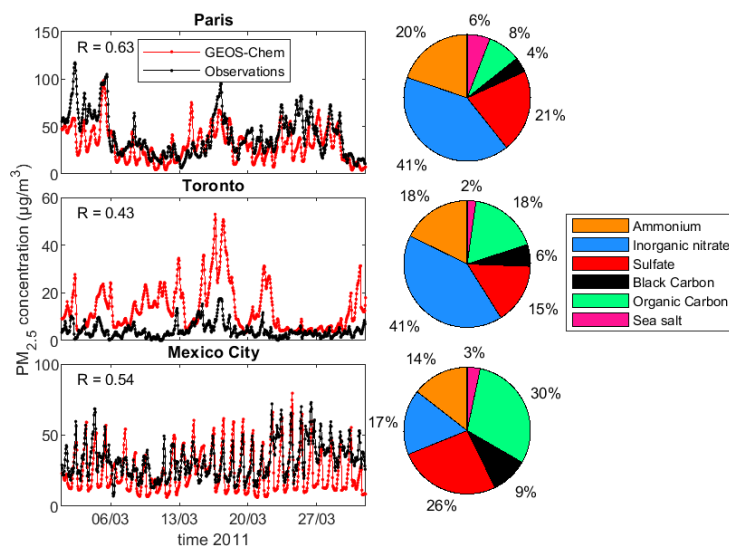


378

379 Figure 8: Left: time-series of daily  $\text{NH}_3$  columns derived from IASI (black lines) and the GEOS-Chem model (red  
 380 lines) over Europe (upper panel), North America (middle panel), and southern North America (lower panel).  
 381 Right: maps of  $\text{NH}_3$  columns (in molecules/ $\text{cm}^2$ ) differences between IASI and GEOS-Chem model for March  
 382 2011.

383 At the city scales of Paris and Mexico City, the daily model  $\text{NH}_3$  columns are in relatively good  
 384 agreements with IASI observations within a 50-km radius circle from the city-centers (not shown  
 385 here), since the coefficient of correlation are  $R = 0.42$  and  $R = 0.52$ , respectively. Similar to the  
 386 regional domains, GEOS-Chem  $\text{NH}_3$  columns are relatively underestimated at the city scales of Paris  
 387 and Mexico City, with a MRD of 14% and 72%. At the city scale of Toronto, the correlation between  
 388 the  $\text{NH}_3$  columns derived from the model and observed by IASI is poor, with a coefficient of  
 389 correlation of  $R = -0.32$ , and an overestimation of the modelled  $\text{NH}_3$  concentrations is found with a  
 390 MRD of -81%.

391 Local comparison of  $\text{PM}_{2.5}$  concentrations at the city scale (over Paris, Toronto, and Mexico) is shown  
 392 in Figure 9, left panels. They show that  $\text{PM}_{2.5}$  concentrations calculated by the model in March 2011  
 393 are in relatively better agreement with the surface observations with  $R = 0.63$ ,  $R = 0.43$ , and  $R = 0.54$   
 394 in Paris, Toronto and Mexico City. In Paris and Mexico City,  $\text{PM}_{2.5}$  concentrations values derived from  
 395 the observations are overall higher than the GOES-Chem concentrations with MRD values of 55% and  
 396 65%, respectively, whereas GEOS-Chem  $\text{PM}_{2.5}$  concentrations are higher than the observations in  
 397 Toronto with MRD value of -59%.



398

399 Figure 9: left: Time-series of hourly PM<sub>2.5</sub> (µg/m<sup>3</sup>) derived from surface observations (black lines) and the GEOS-  
 400 Chem model (red lines) over Paris (upper panel), Toronto (middle panel), and Mexico (lower panel) cities for  
 401 March 2011. Right: PM<sub>2.5</sub> speciation (% in total mass) derived from the GEOS-Chem run for March 2011.

402 The right panels of Figure 9 show the chemical composition of the PM<sub>2.5</sub> from GEOS-Chem. These  
 403 inform us about the different pollution sources. Organic matter sources split equally between the  
 404 primary emissions and the oxidation of volatile organic compounds [Day et al., 2015]. SNA (sum of  
 405 sulfate, nitrate, and ammonium) sources originate in chemical transformation of gaseous precursors  
 406 in the atmosphere, whereas black carbon comes from primary emissions of industrial and traffic  
 407 combustion.

408 According to the GEOS-Chem model, SNA dominates the PM<sub>2.5</sub> chemical composition mass in March  
 409 2011 over the 3 cities, meaning that the dominant source of PM<sub>2.5</sub> mass comes from the secondary  
 410 oxidation path. This partition of SNA in March 2011 from the model is higher than what have been  
 411 reported based on 1-year-measurements performed in 2013: 43%, 42%, and 33% of the PM<sub>2.5</sub> mass  
 412 composition in Paris, Toronto, and Mexico City, respectively [Cheng et al., 2016].

413 In Toronto, PM<sub>2.5</sub> speciation is monitored by the National Air Pollution Surveillance Program (NAPS,  
 414 [https://www.canada.ca/en/environment-climate-change/services/air-pollution/monitoring-  
 415 networks-data/national-air-pollution-program.html](https://www.canada.ca/en/environment-climate-change/services/air-pollution/monitoring-networks-data/national-air-pollution-program.html)) network. Observations in March 2011 reveal  
 416 that inorganic nitrate burden is overestimated by a factor 2 in the GEOS-Chem run (41% in the model  
 417 compared to 20% in the observations), whereas sulfate and black carbon abundances are  
 418 underestimated by a factor 2 (15 and 6% in the model compared to 27 and 12% in the observations).

419 In Mexico City, the organic matter represents the most abundant fraction of the aerosol, which is  
 420 consistent with measurements made during several campaigns performed in the dry season of 2006  
 421 during the Megacity Initiative: Local And Global Research Observations (MILAGRO, [Molina et al.,  
 422 2010]) and Aerosoles en Ciudad Universitaria (ACU) in 2015 [Salcedo et al., 2018]. Daily cycles appear  
 423 overexaggerated in the model with maxima well represented and minima greatly underestimated.





424 This could suggest model issues in term of atmospheric dynamics (removal/transport or planetary  
425 boundary layer dynamics) due to coarseness of grid.

#### 426 **4. Conclusion**

427 The AmmonAQ project aims to determine the impact of intensive agricultural practices on urban  
428 pollution in the Paris, Toronto, and Mexico metropolitan areas. For this purpose, PM<sub>2.5</sub> and NH<sub>3</sub>  
429 measurements from in situ instruments and satellite infrared spectrometers, and atmospheric model  
430 simulations, have been combined.

431 Using 10-years of IASI observations, NH<sub>3</sub> sources regions have been identified. All of the sources are  
432 from the agricultural sector (husbandry and fertilizer application) in the Europe and North America  
433 domains, whereas, some of them are industrial in the southern North America region. Consequently,  
434 the spatio-temporal variability of NH<sub>3</sub> is different, with stronger seasonal variabilities in Europe and  
435 North America. A strong correlation is found between NH<sub>3</sub> total columns and surface temperature  
436 (T<sub>skin</sub>) for all regions, with higher correlation over agricultural regions, and when the temperature  
437 seasonal cycle is pronounced. We find that the timing of the fertilizer application can be detected  
438 through local maxima in the NH<sub>3</sub>/T<sub>skin</sub> relationship curve.

439 According to HYSPLIT cluster analysis, the highest NH<sub>3</sub> concentrations measured at the city scales are  
440 associated with air masses coming from the surrounding regions and the north-northeast of Paris,  
441 the south-southwest of Toronto, and the southeast/southwest of Mexico City. These will lead to the  
442 exacerbation of the degradation of air quality in each of the 3 cities.

443 Pollution episodes are found to be annually frequent at the 3 cities, especially in springtime when  
444 high NH<sub>3</sub> and PM<sub>2.5</sub> are observed. In Paris and Mexico, winds are coming from the northeast-  
445 southwest directions, whereas, in Toronto, the transboundary transport of pollutant from the  
446 United-States is dominant during pollution events.

447 The evaluation of the GEOS-Chem outputs in March 2011 reveals that NH<sub>3</sub> concentrations are overall  
448 underestimated by the model at the regional scale, with, however, a good representability of the  
449 day-to-day variability in Europe and North America domains. NH<sub>3</sub> columns derived from IASI and the  
450 GEOS-Chem model exhibit substantial spatial differences in the Europe and southern North America  
451 areas. In term of PM<sub>2.5</sub> concentrations at the city scales, we show that they are underestimated in  
452 Paris and Mexico, but overestimated in Toronto.

453 The IASI thermal infrared remote sensors have proved to be valuable to monitor pollution events  
454 over cities. The main limitations are associated with the low revisit time (at the beginning and at the  
455 end of the day), the lack of sensitivity to the surface in particular in winter, and some areas are not  
456 well covered during cloudy scenes. In the near future the next generation of instruments will have  
457 improved capabilities to sound deeper in the atmosphere [Crevoisier et al., 2014]. The IRS-MTG  
458 satellite instrument that should be launch in 2024 in geostationary orbit will offer the capacity to  
459 enhance this research over Europe thanks to better temporal (measurements every 30-45 minutes)  
460 and spatial (4 km x 4 km pixel) resolution.

#### 461 **Data availability**

462  
463 The near-real-time IASI NH<sub>3</sub> (ANNI NH<sub>3</sub>-v3) data used in this study are freely available through the  
464 Aeris database <https://iasi.aeris-data.fr/nh3-i/> (Van Damme et al., 2021) (last access: 1 April 2022).  
465 All hourly observations of PM<sub>2.5</sub> concentrations are available from the Airparif network ([https://data-  
466 airparif-asso.opendata.arcgis.com/](https://data-airparif-asso.opendata.arcgis.com/)), the Ministry of the Environment, Conservation and Parks of  
467 Ontario (<http://www.airqualityontario.com/>), and the Red Automática de Monitoreo Atmosférico



468 (RAMA, <http://www.aire.cdmx.gob.mx/default.php?opc=%27aKBh%27>) network (last access: 1 April  
469 2022). The GEOS-Chem outputs are currently available upon request. All MATLAB/PYTHON codes  
470 used to create any of the figures and/or to create the underlying data are available on request.

#### 471 **Author contributions**

472 CV, CC, SY, and KS designed the AmmonAQ project. MV and LC provided the IASI data. WP provided  
473 the GEOS-Chem outputs. CV and RA analyzed the data. CV, RA, and SS wrote the manuscript draft.  
474 BH, MG, KS, P-FC, and CC reviewed and edited the manuscript.

#### 475 **Competing interests**

476 The authors declare that they have no conflict of interest.

#### 477 **Acknowledgments**

478 AmmonAQ results from a joint research program between CNRS (National Center for Scientific  
479 Research of France) and the University of Toronto which funded one year of common research in  
480 2019. Research at ULB was supported by the Belgian State Federal Office for Scientific, Technical and  
481 Cultural Affairs (Prodex HIRS) and the Air Liquide Foundation (TAPIR project). LC is Research  
482 Associate supported by the Belgian F.R.S.-FNRS. This project has received funding from the European  
483 Research Council (ERC) under the European Union's Horizon 2020 and innovation programme (grant  
484 agreement No 742909, IASI-FT advanced ERC grant). The MERRA-2 data used in this study have been  
485 provided by the Global Modeling and Assimilation Office (GMAO) at NASA Goddard Space Flight  
486 Center.

#### 487 **References**

488 Abeed, R., Clerbaux, C., Clarisse, L., Van Damme, M., Coheur, P.-F., Safieddine, S.: A space view of  
489 agricultural and industrial changes during the Syrian civil war, *Elementa: Science of the*  
490 *Anthropocene*, 9(1). doi:<https://doi.org/10.1525/elementa.2021.000041>, 2021

491 Asman, W., Sutton, M. A. and Schjörriing, J. K.: Ammonia: emission, atmospheric transport and  
492 deposition, *New Phytol.*, 139, 27–48, 1998.

493 Bey, I., Jacob, D. J., Yantosca, R. M., Logan, J. A., Field, B. D., Fiore, A. M., Li, Q., Liu, H. Y., Mickley, L. J.  
494 and Schultz, M. G.: Global modeling of tropospheric chemistry with assimilated meteorology: Model  
495 description and evaluation, *J. Geophys. Res. Atmos.*, 106(D19), 23073–23095,  
496 doi:<https://doi.org/10.1029/2001JD000807>, 2001.

497 Bouwman, A. F., Lee, D. S., Asman, W. A. H., Dentener, F. J., Van Der Hoek, K. W. and Olivier, J. G. J.: A  
498 global high-resolution emission inventory for ammonia, *Global Biogeochem. Cycles*, 11(4), 561–587,  
499 doi:<https://doi.org/10.1029/97GB02266>, 1997.

500 Cheng, Z., Luo, L., Wang, S., Wang, Y., Sharma, S., Shimadera, H., Wang, X., Bressi, M., de Miranda, R.  
501 M., Jiang, J., Zhou, W., Fajardo, O., Yan, N. and Hao, J.: Status and characteristics of ambient PM<sub>2.5</sub>  
502 pollution in global megacities, *Environ. Int.*, 89–90, 212–221,  
503 doi:<https://doi.org/10.1016/j.envint.2016.02.003>, 2016.



- 504 Clerbaux, C., Boynard, A., Clarisse, L., George, M., Hadji-Lazaro, J., Herbin, H., Hurtmans, D., Pommier,  
505 M., Razavi, A., Turquety, S., Wespes, C. and Coheur, P.-F.: Monitoring of atmospheric composition  
506 using the thermal infrared IASI/MetOp sounder, *Atmos. Chem. Phys.*, 9(16), 6041–6054,  
507 doi:10.5194/acp-9-6041-2009, 2009.
- 508 Crevoisier, C., Clerbaux, C., Guidard, V., Phulpin, T., Armante, R., Barret, B., Camy-Peyret, C.,  
509 Chaboureaud, J.-P., Coheur, P.-F., Crépeau, L., Dufour, G., Labonnote, L., Lavanant, L., Hadji-Lazaro, J.,  
510 Herbin, H., Jacquinet-Husson, N., Payan, S., Péquignot, E., Pierangelo, C., Sellitto, P., and  
511 Stubenrauch, C.: Towards IASI-New Generation (IASI-NG): impact of improved spectral resolution and  
512 radiometric noise on the retrieval of thermodynamic, chemistry and climate variables, *Atmos. Meas.*  
513 *Tech.*, 7, 4367–4385, <https://doi.org/10.5194/amt-7-4367-2014>, 2014.
- 514 Day, M. C., Zhang, M. and Pandis, S. N.: Evaluation of the ability of the EC tracer method to estimate  
515 secondary organic carbon, *Atmos. Environ.*, 112, 317–325,  
516 doi:<https://doi.org/10.1016/j.atmosenv.2015.04.044>, 2015.
- 517 Fountoukis, C. and Nenes, A.: ISORROPIA II: a computationally efficient thermodynamic equilibrium  
518 model for  $K^+$ – $Ca^{2+}$ – $Mg^{2+}$ – $NH_4^+$ – $Na^+$ – $SO_4^{2-}$ – $NO_3^-$ – $Cl^-$ – $H_2O$  aerosols, *Atmos. Chem. Phys.*, 7,  
519 4639–4659, <https://doi.org/10.5194/acp-7-4639-2007>, 2007.
- 520 Guo, X., Wang, R., Pan, D., Zondlo, M. A., Clarisse, L., Van Damme, M., Whitburn, S., Coheur, P.-F.,  
521 Clerbaux, C., Franco, B., Golston, L. M., Wendt, L., Sun, K., Tao, L., Miller, D., Mikoviny, T., Müller, M.,  
522 Wisthaler, A., Tevlin, A. G., Murphy, J. G., Nowak, J. B., Roscioli, J. R., Volkamer, R., Kille, N., Neuman,  
523 J. A., Eilerman, S. J., Crawford, J. H., Yacovitch, T. I., Barrick, J. D. and Scarino, A. J.: Validation of IASI  
524 Satellite Ammonia Observations at the Pixel Scale Using In Situ Vertical Profiles, *J. Geophys. Res.*  
525 *Atmos.*, 126(9), e2020JD033475, doi:<https://doi.org/10.1029/2020JD033475>, 2021.
- 526 Herrera B, et al.: Evolution and distribution of  $NH_3$  over Mexico City from ground-based and satellite  
527 infrared spectroscopic measurements, in prep., 2022.
- 528 Hersbach, H.; Bell, B.; Berrisford, P.; Hirahara, S.; Horányi, A.; Muñoz-Sabater, J.; Nicolas, J.; Peubey,  
529 C.; Radu, R.; Schepers, D.; et al. The ERA5 global reanalysis. *Q. J. R. Meteorol. Soc.* **2020**, *146*, 1999–  
530 2049, doi:10.1002/qj.3803.
- 531 Hoesly, R. M., Smith, S. J., Feng, L., Klimont, Z., Janssens-Maenhout, G., Pitkanen, T., Seibert, J. J., Vu,  
532 L., Andres, R. J., Bolt, R. M., Bond, T. C., Dawidowski, L., Kholod, N., Kurokawa, J.-I., Li, M., Liu, L., Lu,  
533 Z., Moura, M. C. P., O'Rourke, P. R. and Zhang, Q.: Historical (1750–2014) anthropogenic emissions of  
534 reactive gases and aerosols from the Community Emissions Data System (CEDs), *Geosci. Model Dev.*,  
535 11(1), 369–408, doi:10.5194/gmd-11-369-2018, 2018.
- 536 INECC and SEMARNAT 2018 México, Secretaría del Medio Ambiente de la Ciudad de México.  
537 Inventario de Emisiones de la Ciudad de México 2016. Dirección General de Gestión de la Calidad del  
538 Aire, Dirección de Programas de Calidad del Aire e Inventario de Emisiones. Ciudad de México.  
539 Septiembre, 2018 ([http://www.aire.cdmx.gob.mx/descargas/publicaciones/flippingbook/inventario-](http://www.aire.cdmx.gob.mx/descargas/publicaciones/flippingbook/inventario-emisiones-2016/mobile/inventario-emisiones-2016.pdf)  
540 [emisiones-2016/mobile/inventario-emisiones-2016.pdf](http://www.aire.cdmx.gob.mx/descargas/publicaciones/flippingbook/inventario-emisiones-2016/mobile/inventario-emisiones-2016.pdf), last access May 28 2021).



- 541 Jeong, C.-H., Traub, A., Huang, A., Hilker, N., Wang, J. M., Herod, D., Dabek-Zlotorzynska, E., Celo, V.  
542 and Evans, G. J.: Long-term analysis of PM<sub>2.5</sub> from 2004 to 2017 in Toronto: Composition, sources,  
543 and oxidative potential, *Environ. Pollut.*, 263, 114652,  
544 doi:<https://doi.org/10.1016/j.envpol.2020.114652>, 2020.
- 545 Karydis, V. A., Tsimpidi, A. P., Lei, W., Molina, L. T., and Pandis, S. N.: Formation of semi volatile  
546 inorganic aerosols in the Mexico City Metropolitan Area during the MILAGRO campaign, *Atmos.*  
547 *Chem. Phys.*, 11, 13305–13323, <https://doi.org/10.5194/acp-11-13305-2011>, 2011.
- 548 Larios, A. D., Chebana, F., Godbout, S., Brar, S. K., Valera, F., Palacios, J. H., Avalos Ramirez, A.,  
549 Saldoval-Salas, F., Larouche, J. P., Medina-Hernández, D. and Potvin, L.: Analysis of atmospheric  
550 ammonia concentration from four sites in Quebec City region over 2010–2013, *Atmos. Pollut. Res.*,  
551 9(3), 476–482, doi:<https://doi.org/10.1016/j.apr.2017.11.001>, 2018.
- 552 Lee, P. K. H., Brook, J. R., Dabek-Zlotorzynska, E. and Mabury, S. A.: Identification of the Major  
553 Sources Contributing to PM<sub>2.5</sub> Observed in Toronto, *Environ. Sci. Technol.*, 37(21), 4831–4840,  
554 doi:10.1021/es026473i, 2003.
- 555 McDuffie, E. E., Martin, R. V., Spadaro, J. V., Burnett, R., Smith, S. J., O'Rourke, P., Hammer, M. S., van  
556 Donkelaar, A., Bindle, L., Shah, V., Jaeglé, L., Luo, G., Yu, F., Adeniran, J. A., Lin, J. and Brauer, M.:  
557 Source sector and fuel contributions to ambient PM<sub>2.5</sub> and attributable mortality across multiple  
558 spatial scales, *Nat. Commun.*, 12(1), 3594, doi:10.1038/s41467-021-23853-y, 2021.
- 559 Molina, L. T., Madronich, S., Gaffney, J. S., Apel, E., de Foy, B., Fast, J., Ferrare, R., Herndon, S.,  
560 Jimenez, J. L., Lamb, B., Osornio-Vargas, A. R., Russell, P., Schauer, J. J., Stevens, P. S., Volkamer, R., &  
561 Zavala, M. (2010). An overview of the MILAGRO 2006 Campaign: Mexico City emissions and their  
562 transport and transformation. *Atmospheric Chemistry and Physics*, 10(18), 8697–8760.  
563 <https://doi.org/10.5194/acp-10-8697-2010>
- 564 Moya, M., Fountoukis, C., Nenes, A., Matías, E., and Grutter, M.: Predicting diurnal variability of fine  
565 inorganic aerosols and their gas-phase precursors near downtown Mexico City, *Atmos. Chem. Phys.*  
566 *Discuss.*, 7, 11257–11294, <https://doi.org/10.5194/acpd-7-11257-2007>, 2007.
- 567 Murray, C. J. L., Aravkin, A. Y., Zheng, P., Abbafati, C., Abbas, K. M., Abbasi-Kangevari, M., Abd-Allah,  
568 F., Abdelalim, A., Abdollahi, M., Abdollahpour, I., Abegaz, K. H., Abolhassani, H., Aboyans, V., Abreu,  
569 L. G., Abrigo, M. R. M., Abualhasan, A., Abu-Raddad, L. J., Abushouk, A. I., Adabi, M., Adekanmbi, V.,  
570 Adeoye, A. M., Adetokunboh, O. O., Adham, D., Advani, S. M., Agarwal, G., Aghamir, S. M. K.,  
571 Agrawal, A., Ahmad, T., Ahmadi, K., Ahmadi, M., Ahmadi, H., Ahmed, M. B., Akalu, T. Y., Akinyemi,  
572 R. O., Akinyemiju, T., Akombi, B., Akunna, C. J., Alahdab, F., Al-Aly, Z., Alam, K., Alam, S., Alam, T.,  
573 Alanezi, F. M., Alanzi, T. M., Alemu, B. wassihun, Alhabib, K. F., Ali, M., Ali, S., Alicandro, G., Alinia, C.,  
574 Alipour, V., Alizade, H., Aljunid, S. M., Alla, F., Allebeck, P., Almasi-Hashiani, A., Al-Mekhlafi, H. M.,  
575 Alonso, J., Altirkawi, K. A., Amini-Rarani, M., Amiri, F., Amugsi, D. A., Ancuceanu, R., Anderlini, D.,  
576 Anderson, J. A., Andrei, C. L., Andrei, T., Angus, C., Anjomshoa, M., Ansari, F., Ansari-Moghaddam, A.,  
577 Antonazzo, I. C., Antonio, C. A. T., Antony, C. M., Antriyandarti, E., Anvari, D., Anwer, R., Appiah, S. C.  
578 Y., Arabloo, J., Arab-Zozani, M., Ariani, F., Armoon, B., Ärnlov, J., Arzani, A., Asadi-Aliabadi, M., Asadi-  
579 Pooya, A. A., Ashbaugh, C., Assmus, M., Atafar, Z., Atnafu, D. D., Atout, M. M. W., Ausloos, F.,  
580 Ausloos, M., Ayala Quintanilla, B. P., Ayano, G., Ayanore, M. A., Azari, S., Azarian, G., Azene, Z. N., et



- 581 al.: Global burden of 87 risk factors in 204 countries and territories, 1990&#x2013;2019: a systematic  
582 analysis for the Global Burden of Disease Study 2019, *Lancet*, 396(10258), 1223–1249,  
583 doi:10.1016/S0140-6736(20)30752-2, 2020.
- 584 Nair, A. A. and Yu, F.: Quantification of Atmospheric Ammonia Concentrations: A Review of Its  
585 Measurement and Modeling, *Atmosphere (Basel)*, 11(10), doi:10.3390/atmos11101092, 2020.
- 586 Ojeda-Castillo, V., Alonso-Romero, S., Mena, L. H.-, Álvarez-Chávez, P. E. and del Real-Olvera, J.: Air  
587 Pollution in an Urban Area of Mexico: Sources of Emission (Vehicular, Natural, Industrial, and Brick  
588 Production), in *Air Pollution*, edited by J. D. R. Olvera, IntechOpen, Rijeka., 2019.
- 589 Pai, S. J., Heald, C. L., Pierce, J. R., Farina, S. C., Marais, E. A., Jimenez, J. L., Campuzano-Jost, P., Nault,  
590 B. A., Middlebrook, A. M., Coe, H., Shilling, J. E., Bahreini, R., Dingle, J. H. and Vu, K.: An evaluation of  
591 global organic aerosol schemes using airborne observations, *Atmos. Chem. Phys.*, 20(5), 2637–2665,  
592 doi:10.5194/acp-20-2637-2020, 2020.
- 593 Paulot, F. and Jacob, D. J.: Hidden Cost of U.S. Agricultural Exports: Particulate Matter from Ammonia  
594 Emissions, *Environ. Sci. Technol.*, 48(2), 903–908, doi:10.1021/es4034793, 2014.
- 595 Potter, P., Ramankutty, N., Bennett, E. M., & Donner, S. D. (2010). Characterizing the Spatial Patterns  
596 of Global Fertilizer Application and Manure Production. *Earth Interactions*, 14(2), 1–22.  
597 <https://doi.org/10.1175/2009EI288.1>
- 598 RANDERSON, J. T., VAN DER WERF, G. R., GIGLIO, L., COLLATZ, G. J. and KASIBHATLA, P. S.: Global Fire  
599 Emissions Database, Version 4.1 (GFEDv4), , doi:10.3334/ORNLDAAC/1293, 2017.
- 600 Retama, A., Neria-Hernández, A., Jaimes-Palomera, M., Rivera-Hernández, O., Sánchez-Rodríguez, M.,  
601 López-Medina, A. and Velasco, E.: Fireworks: A major source of inorganic and organic aerosols during  
602 Christmas and New Year in Mexico City, *Atmos. Environ.* X, 2, 100013,  
603 doi:<https://doi.org/10.1016/j.aeaoa.2019.100013>, 2019.
- 604 REYNOLDS, C. M. and WOLF, D. C.: EFFECT OF SOIL MOISTURE AND AIR RELATIVE HUMIDITY ON  
605 AMMONIA VOLATILIZATION FROM SURFACE-APPLIED UREA, *Soil Sci.*, 143(2) [online] Available from:  
606 [https://journals.lww.com/soilsci/Fulltext/1987/02000/EFFECT\\_OF\\_SOIL\\_MOISTURE\\_AND\\_AIR\\_RELAT](https://journals.lww.com/soilsci/Fulltext/1987/02000/EFFECT_OF_SOIL_MOISTURE_AND_AIR_RELATIVE_HUMIDITY.10.aspx)  
607 [IVE\\_HUMIDITY.10.aspx](https://journals.lww.com/soilsci/Fulltext/1987/02000/EFFECT_OF_SOIL_MOISTURE_AND_AIR_RELATIVE_HUMIDITY.10.aspx), 1987.
- 608 Salcedo, D., Alvarez-Ospina, H., Peralta, O., & Castro, T. (2018). PM1 Chemical Characterization  
609 during the ACU15 Campaign, South of Mexico City. *Atmosphere*, 9(6).  
610 <https://doi.org/10.3390/atmos9060232>
- 611 Secretaría del Medio Ambiente de la Ciudad de México. Calidad del aire en la Ciudad de México,  
612 Informe 2018. [Internet]. Dirección General de Calidad del Aire, Dirección de Monitoreo de Calidad  
613 del Aire: Ciudad de México; 2020. Available from:  
614 <http://www.aire.cdmx.gob.mx/default.php?opc=Z6Bhnml>.



- 615 Stein, A. F., Draxler, R. R., Rolph, G. D., Stunder, B. J. B., Cohen, M. D. and Ngan, F.: NOAA's HYSPLIT  
616 Atmospheric Transport and Dispersion Modeling System, *Bull. Am. Meteorol. Soc.*, 96(12), 2059–  
617 2077, doi:10.1175/BAMS-D-14-00110.1, 2015.
- 618 Sutton, M. A., Reis, S., Riddick, S. N., Dragosits, U., Nemitz, E., Theobald, M. R., Tang, Y. S., Braban, C.  
619 F., Vieno, M., Dore, A. J., Mitchell, R. F., Wanless, S., Daunt, F., Fowler, D., Blackall, T. D., Milford, C.,  
620 Flechard, C. R., Loubet, B., Massad, R., Cellier, P., Personne, E., Coheur, P. F., Clarisse, L., Van Damme,  
621 M., Ngadi, Y., Clerbaux, C., Skjøth, C. A., Geels, C., Hertel, O., Wichink Kruit, R. J., Pinder, R. W., Bash,  
622 J. O., Walker, J. T., Simpson, D., Horváth, L., Misselbrook, T. H., Bleeker, A., Dentener, F. and de Vries,  
623 W.: Towards a climate-dependent paradigm of ammonia emission and deposition, *Philos. Trans. R.  
624 Soc. Lond. B. Biol. Sci.*, 368(1621), 20130166, doi:10.1098/rstb.2013.0166, 2013.
- 625 von Bobruzki, K., Braban, C. F., Famulari, D., Jones, S. K., Blackall, T., Smith, T. E. L., Blom, M., Coe, H.,  
626 Gallagher, M., Ghalaieny, M., McGillen, M. R., Percival, C. J., Whitehead, J. D., Ellis, R., Murphy, J.,  
627 Mohacsi, A., Pogany, A., Junninen, H., Rantanen, S., Sutton, M. A. and Nemitz, E.: Field inter-  
628 comparison of eleven atmospheric ammonia measurement techniques, *Atmos. Meas. Tech.*, 3(1),  
629 91–112, doi:10.5194/amt-3-91-2010, 2010.
- 630 Van Damme, M., Clarisse, L., Franco, B., Sutton, M. A., Erisman, J. W., Wichink Kruit, R., van Zanten,  
631 M., Whitburn, S., Hadji-Lazaro, J., Hurtmans, D., Clerbaux, C., & Coheur, P.-F.: Global, regional and  
632 national trends of atmospheric ammonia derived from a decadal (2008–2018) satellite record.  
633 *Environmental Research Letters*, 16(5), 55017. <https://doi.org/10.1088/1748-9326/abd5e0>, 2021.
- 634 Van Damme, M., Clarisse, L., Whitburn, S., Hadji-Lazaro, J., Hurtmans, D., Clerbaux, C. and Coheur, P.-  
635 F.: Industrial and agricultural ammonia point sources exposed, *Nature*, 564(7734), 99–103,  
636 doi:10.1038/s41586-018-0747-1, 2018.
- 637 Van Damme, M., Whitburn, S., Clarisse, L., Clerbaux, C., Hurtmans, D., and Coheur, P.-F.: Version 2 of  
638 the IASI NH<sub>3</sub> neural network retrieval algorithm: near-real-time and reanalysed datasets, *Atmos.  
639 Meas. Tech.*, 10, 4905–4914, <https://doi.org/10.5194/amt-10-4905-2017>, 2017.
- 640 Vega, E., Eidels, S., Ruiz, H., López-Veneroni, D., Sosa, G., Gonzalez, E., Watson, J. G., Edgerton, S. A.,  
641 Gasca, J., Mora, V., Reyes, E., Sánchez-Reyna, G., Villaseñor, R. and Chow, J. C.: Particulate Air  
642 Pollution in Mexico City: A Detailed View, *Aerosol Air Qual. Res.*, 10(3), 193–211,  
643 doi:10.4209/aaqr.2009.06.0042, 2010.
- 644 Viatte, C., Petit, J.-E., Yamanouchi, S., Van Damme, M., Doucerain, C., Germain-Piaulenne, E., Gros,  
645 V., Favez, O., Clarisse, L., Coheur, P.-F., Strong, K. and Clerbaux, C.: Ammonia and PM<sub>2.5</sub> air pollution  
646 in paris during the 2020 covid lockdown, *Atmosphere (Basel)*, 12(2), doi:10.3390/atmos12020160,  
647 2021.
- 648 Viatte, C., Wang, T., Van Damme, M., Dammers, E., Meleux, F., Clarisse, L., Shephard, M. W.,  
649 Whitburn, S., François Coheur, P., Cady-Pereira, K. E. and Clerbaux, C.: Atmospheric ammonia  
650 variability and link with particulate matter formation: A case study over the Paris area, *Atmos. Chem.  
651 Phys.*, 20(1), doi:10.5194/acp-20-577-2020, 2020.



- 652 Wang, Q., Jacob, D. J., Spackman, J. R., Perring, A. E., Schwarz, J. P., Moteki, N., Marais, E. A., Ge, C.,  
653 Wang, J. and Barrett, S. R. H.: Global budget and radiative forcing of black carbon aerosol: Constraints  
654 from pole-to-pole (HIPPO) observations across the Pacific, *J. Geophys. Res. Atmos.*, 119(1), 195–206,  
655 doi:<https://doi.org/10.1002/2013JD020824>, 2014.
- 656 Yamanouchi, S., Viatte, C., Strong, K., Lutsch, E., Jones, D. B. A., Clerbaux, C., Van Damme, M.,  
657 Clarisse, L., and Coheur, P.-F.: Multiscale observations of NH<sub>3</sub> around Toronto, Canada, *Atmos. Meas.*  
658 *Tech.*, 14, 905–921, <https://doi.org/10.5194/amt-14-905-2021>, 2021.
- 659 Yao, X. and Zhang, L.: Causes of Large Increases in Atmospheric Ammonia in the Last Decade across  
660 North America, *ACS omega*, 4(26), 22133–22142, doi:10.1021/acsomega.9b03284, 2019.
- 661 Zellweger, C., Hüglin, C., Klausen, J., Steinbacher, M., Vollmer, M., and Buchmann, B.: Inter-  
662 comparison of four different carbon monoxide measurement techniques and evaluation of the long-  
663 term carbon monoxide time series of Jungfraujoch, *Atmos. Chem. Phys.*, 9, 3491–3503,  
664 <https://doi.org/10.5194/acp-9-3491-2009>, 2009.